Intervalley Excitonic Hybridization, Optical Selection Rules, and Imperfect Circular Dichroism in Monolayer math xmlns="http://www.w3.org/1998/Math/MathML" display="inline">mrow>mi>h/mi>mtext>−/mtext>mi>BN /mi>/mrow>/math>

Fang Zhang, Chin Shen Ong, Jia Wei Ruan, Meng Wu, Xing Qiang Shi, Zi Kang Tang, and Steven G. Louie

Phys. Rev. Lett. **128**, 047402 — Published 27 January 2022

DOI: 10.1103/PhysRevLett.128.047402

Intervalley excitonic hybridization, optical selection rules, and imperfect circular dichroism in monolayer hBN

Fang Zhang[1,2,3,4], Chin Shen Ong[2,3], Jia Wei Ruan[2,3], Meng Wu[2,3], Xing Qiang Shi[4], Zi Kang Tang[1,*] and Steven G. Louie[2,3,*]

[1]*Institute of Applied Physics and Materials Engineering, University of Macau, Macau S.A.R. 999078, China.*

[2]*Department of Physics, University of California at Berkeley, California 94720, USA.*

[3]*Materials Sciences Division, Lawrence Berkeley National Laboratory, California 94720, USA*

[4]*Department of Physics, Southern University of Science and Technology, ShenZhen 518000, China.*

**Email:* zktang@um.edu.mo; sglouie@berkeley.edu

Abstract

We perform first-principles *GW* plus Bethe-Salpeter equation calculations to investigate the photophysics of monolayer hexagonal boron nitride (hBN), revealing excitons with novel **k**-space characteristics. The excitonic states forming the first and third peaks in its absorption spectrum are *s*-like, but those of the second peak is notably *p*-like, a first finding of strong co-occurrence of bright *s*-like and bright *p*-like states in an intrinsic 2D material. Moreover, even though the **k**-space wavefunction of these excitonic states are centered at the *K*- and K'-valleys like in monolayer transition metal dichalcogenides, the **k**-space envelope functions of the basis excitons at one valley have significant extents to the basin of the other valley. As a consequence, the optical response of monolayer hBN exhibits a lack of circular dichroism, as well as a coupling that induces an intervalley mixing between *s*- and *p*-like states.

Main text

Atomically thin two-dimensional (2D) semiconductors, such as gapped graphene systems [1-2] and monolayer transition-metal dichalcogenides (TMDs) [3-5], with honeycomb-like crystal structure and broken inversion symmetry, are of great interest due to their novel physical properties. Their low-energy optical absorption is dominated by the excitation of bound electron-hole pairs that are highly localized in **k**-space, namely, Wannier excitons. The excitons from different valleys are commonly viewed as independent or known to be extremely weakly interacting with each other, and the highly **k**-space localized nature of them has led to a series of discoveries, such as new optical selection rules due to non-trivial band topology and valley exciton circular dichroism [6-7].

However, both gapped graphene systems and mono- or few-layer TMDs are semiconductors with relatively small quasiparticle (QP) bandgaps, *e.g.*, of a few hundred meVs in biased bilayer graphene [8] and in the range of 2.6 eV to 2.8 eV in monolayer MoS_2 [9-11]. For 2D wide bandgap *insulators*, dielectric screening is much weaker than that in 2D semiconductors [12]. A large bandgap also leads to less dispersive bands with larger effective masses, which together with the reduced screening result in coupling of free electron-hole pairs over a large area of the Brillouin zone (BZ) and a large increase in the binding energy of the low-lying bound excitons. Unlike the extensive investigation of Wannier excitons in 2D semiconductors, the excitonic properties of 2D insulators are less studied [13] although a number of dark *p*-like exciton features were presented [14]. Whereas to date, 2D insulators, such as 2D hexagonal boron nitride (hBN), play a pivotal role in the fabrication of moiré heterostructures [15-17] and in usages of ultra-violet photophysics [18] and quantum emission [19].

In this work, we have explored the excitonic properties of monolayer hBN employing the *ab initio GW* and *GW* plus Bethe-Salpeter equation (*GW*-BSE) approaches [12,20]. We find that monolayer hBN possesses strongly bound excitons with novel **k**-space characteristics, although they can still be identified by their dominant C_3-rotational features. In particular, the first and third peaks in the optical absorption spectrum correspond to *s*-like excitons while the second peak originates from the excitation of *p*-like states (see Fig. 1). To our knowledge, this is the first known case of co-existence of both strongly bright *s*- and bright *p*-like excitons for an intrinsic monolayer 2D material. Moreover, we find that even though these bright excitons are still centered at the K- or K'-valley, their envelope functions are highly non-localized with arms extending far from the K- or K'-point in the BZ. The mixing of the interband electron-hole excitations away from the bottom of a specific valley results in: (1) the absence of perfect circular dichroism; and (2) interactions between *s*- and *p*-like excitons from different valleys. These effects, so far, have not been well identified in honeycomb-like structured 2D materials in the literature.

In Fig. 1(a), we plot the band structure calculated using density-functional theory (DFT) with the Perdew-Burke-Ernzerhof (PBE) exchange-correlation functional [21] and that calculated with the full frequency eigenvalue-self-consistent *GW* approach. At the DFT-PBE level, monolayer hBN is predicted with a direct bandgap at the K-point in the BZ of 4.70 eV, which is much smaller than the *GW* direct bandgap at K of 8.03 eV, owing to strong self-energy effects. Moreover, at the *GW* level, monolayer hBN is an indirect gap insulator with a K-to-Γ indirect gap of 7.45 eV. The calculated absorption spectrum *for linear polarized light* is plotted in Fig. 1(b). There are three main peaks, labeled as *A*, *B* and *C* with excitation energies of 5.95 eV, 6.82 eV and 7.06 eV, respectively. The calculated position of the first peak is in excellent agreement with the measured absorption value of 6.03 eV [22]. These peaks are formed by degenerate excitons as monolayer hBN is a non-centrosymmetric crystal with minimum direct energy gaps of equal value at two valleys, K and K', which are related by time-reversal symmetry. The binding energy of the bright excitons contributing to peak *A* is calculated to be 2.08 eV, which is more than twice that of the lowest energy bright exciton in typical semiconducting monolayer TMDs (*e.g.,* it is 0.65 eV for MoS_2 [9]). The huge binding energy in monolayer hBN is the combined effect of reduced dimensionality [9, 23-24] and large bandgap [12, 25] [see computational details, along with comparison with previous theoretical works in the Supplemental Material (SM) [26] Sec. I].

Now, we examine the characters of the excitons giving rise to the three peaks. The exciton wave functions are obtained by solving the BSE of the interacting two-particle Green's function [12, 30]

$$\left(E^{QP}_{c,\boldsymbol{k}} - E^{QP}_{v,\boldsymbol{k}}\right)A^{S}_{vc\boldsymbol{k}} + \sum\nolimits_{v'c'\boldsymbol{k}'} \langle vc\boldsymbol{k}|K^{eh}|v'c'\boldsymbol{k}'\rangle A^{S}_{v'c'\boldsymbol{k}'} = \Omega_S A^{S}_{vc\boldsymbol{k}} \quad (1)$$

where $E^{QP}_{c,\boldsymbol{k}}$ and $E^{QP}_{v,\boldsymbol{k}}$ are QP energies of an electron in the conduction band and negative of the QP energy of a hole in the valence band as reference to a common chemical potential that is set to zero. $|vc\boldsymbol{k}\rangle$ corresponds to a free electron-hole pair at the point $\boldsymbol{k}$. K^{eh} is the electron-hole interaction kernel, containing a direct electron-hole attractive screened Coulomb term and a repulsive exchange bare Coulomb term [12]. Ω_S is the excitation energy of the exciton state $|S\rangle$, and $A^{S}_{vc\boldsymbol{k}}$ describes the **k**-space exciton envelope function. In our study, we firstly solved Eq. (1) by zeroing out the BSE matrix elements outside of a radius of 1.13 Å^{-1} from the bottom point of the K-valley (we call the solutions at this stage single-valley excitons). By doing so, we only include mixing of interband transitions around the K-valley as the distance between K- and K'-points is 1.66 Å^{-1}. For this calculation, we use a **k**-point sampling grid of 400 × 400 × 1 for the full BZ, and the highest valence and lowest conduction bands only (band indices can thus be omitted in describing the exciton envelope function, i.e., with just $A^{S}_{\boldsymbol{k}}$). In Fig. 2, we plot the amplitude and the phase of A^{S}_{k} for the first four lowest energy singlet excitons, with the K-point set as the origin. The gauge arbitrariness of the computed $A^{S}_{\boldsymbol{k}}$ is eliminated by introducing a gauge requiring the **k**-dependent

phase of the lowest-energy exciton to be smooth, resulting in a rotational quantum number of $m = 0$ for this exciton [Fig. 2(e)]. For the lowest-energy exciton, which is optically bright with linear polarized light (peak *A*), the amplitude of A_k^S has deviations from azimuthal invariance and exhibits a strong trigonal warping, with long arms stretching along the K-to-M directions, consistent with a three-fold rotational symmetry of the system [Fig. 2(a)]. For the second lowest energy exciton which is also bright, giving rise to peak *B*, the phase of its $A_{\boldsymbol{k}}^S$ plotted in Fig. 2(f) has a phase winding pattern that corresponds to an angular quantum number of $m = 1$, indicating that it is 2*p*-like. Also, its amplitude has lobed structures [Fig. 2(b)], the characteristic of hydrogen-like *p*-state wavefunction in a crystal field [31]. We find that the third lowest energy exciton with $m = -1$ is an optically inactive 2*p*-like state [Figs. 2(c) and 2(g)]. For the bright exciton forming peak *C*, a character of a 2*s*-like state is clearly seen in Figs. 2(d) and 2(e). For instance, it has a node in its amplitude that forms a dark circular ring with radius around 0.25 Å^{-1} in Fig. 2(d), and the phase of $A_{\boldsymbol{k}}^S$ from the inside to the outside of the nodal circle changes by π with an angular momentum character of $m = 0$. In summary, by restricting the solutions to basically only one valley, the *bright* singlet excitons forming peaks *A*, *B* and *C* are 1*s*-, 2*p*- and 2*s*-like states, respectively [46].

These bright singlet excitonic states here conform to the optical selection rules first derived in Ref. [6] by Cao, Wu and Louie (CWL), i.e., $m = -l_{\pm} \pmod n$, for a 2D insulator with n-fold rotational symmetry. Here, $l_{\pm}$ denotes the winding number of the interband optical matrix element $\boldsymbol{e}_{\pm} \cdot \langle v\boldsymbol{k}|\hat{v}|c\boldsymbol{k}\rangle$, corresponding to the coupling to $\sigma_{\pm}$ polarized photon modes. The CWL selection rules make use of the topological invariants, l_+ and l_-, that are characteristic of 2D insulating materials. For the lowest conduction band and highest valence band around the K-valley in monolayer hBN, $l_+ = 0$ and $l_- = -1$ (SM Sec. II), and the system has $n = 3$ from the three-fold rotational symmetry. According to the CWL selections rules, for the K-valley, $l_+ = 0$ gives rise to optically active 1*s*- and 2*s*-like states ($m = 0$) in σ_+ polarized light, while $l_- = -1$ ensures the allowed excitation of one of the 2*p*-like states ($m = 1$) by σ_- polarization. The time-reversed criteria apply for the K'-valley derived excitons. Note that while the CWL selection rules make clear which excitations are forbidden, they do not predict quantitively the oscillator strength of those allowed excitations. For monolayer TMDs, within a massive Dirac fermion model, the excitation of 2*p*-like exciton is also selection-allowed [47]. Nonetheless, it is not experimentally observed due to its extremely small oscillator strength [48]. The reason for the drastic difference between monolayer hBN and monolayer TMDs is that hBN has a larger trigonal warping effect than typical TMDs, and we find that the degree of trigonal warping is positively correlated to the oscillator strength of the 2*p*-like exciton (SM Sec. III). The strong trigonal warping of the 2*p*-like exciton (as well as the *s*-like excitons) in monolayer hBN is reflected in the distinct three-fold rotation symmetry seen in its envelope functions (Fig. 2).

Unlike excitons in common monolayer TMDs that are of Wannier type with **k**-space wavefunction localized at the bottoms of the two valleys, the single-valley excitons in hBN have **k**-space wavefunctions that are highly non-localized despite still being centered at K or K'. The blue dashed ring in Fig. 2(a) has a radius of 1/3 in units of $2\pi/a$ (a is the lattice constant of 2.509 Å), which is half the distance between K and K'. Outside of the blue dashed ring, the magnitude of $A_{\boldsymbol{k}}^S$ from the single-patch calculation is still considerably large outside of the K-valley, resulting in mixing of interband transitions from the two valleys once both valleys are taken into consideration. The true exciton envelope function is composed of coupling of transitions between the flat bands along fully in the *K*-*M* high-symmetry directions. This leads to the loss of distinct chirality associated with transitions restricted to an individual valley, resulting in the absence of perfect circular dichroism in the optical response of monolayer hBN. In typical monolayer TMDs, *e.g.* monolayer MoS_2, for most purposes, one can think of the excitons as being time-reversed pair of nearly independent excitonic states localized separately and isolated at either the bottom of the K- or K'-valley, with distinct chirality. As a result, polarization-resolved photoluminescence (PL) spectrum of MoS_2 exhibit circular dichroism (or valley polarization), namely when excited by σ_+ (σ_-) radiation, the polarization of

light from luminescence is basically purely σ_+ (σ_-). The helicity parameter ρ, as defined by $[I(\sigma_+) - I(\sigma_-)]/[I(\sigma_+) + I(\sigma_-)]$ where I denotes intensity, is virtually 1 (-1), as confirmed by experiment [49]. On the other hand, in monolayer hBN, a similar excitation by circularly polarized light will lead to excitation composed of interband electron-hole pairs from a large part of the BZ, including contributions from the other valley. Thus, our *GW*-BSE theory predicts that the luminescence exhibits both σ_+ and σ_- components. Our results give a value of $|\rho|$ equals to 0.78, 0.62 and 0.75 for photon energy corresponding to peak *A*, *B* and *C*, respectively (SM Sec. IV).

Because of intervalley coupling, strictly speaking, one cannot classify the true excitons in hBN in terms of hydrogenic/Rydberg-like states, but as demonstrated below we can still approximately do so. To theoretical analysis, one can expand the *true exciton states* ψ_i of monolayer hBN in terms of some basis excitonic states ϕ_K^j and $\phi_{K'}^l$, that are derived from restricting the basis excitons being composed of transitions from either the K or K' region as in a "patch" calculation (which are the single-valley excitons). That is, $\psi_i = \sum_{j,l}(C_{K,j}^i \phi_K^j + C_{K',l}^i \phi_{K'}^l)$ where j and l denote the quantum numbers of the K and K' basis excitons, respectively. Such a coupling between the basis excitons ϕ_K^j and $\phi_{K'}^l$ (derived from K- and K'-valleys) is naturally included in our complete theory when the full BSE Hamiltonian is solved. Given our finding of the non-localized nature of the true excitons ψ_i in **k**-space, this intervalley interaction (that is nonzero values for the off-diagonal coefficients C) may, in fact, be significant for some states. According to symmetry analysis [14], 1*s*-like basis exciton ϕ_K^{1s} with its time-reversal counterpart $\phi_{K'}^{1s}$ form two orthogonal basis functions of the two-dimensional irreducible representation E of the crystal symmetry: the basis exciton in the K- (K'-) valley belongs to E_+ (E_-) component with $e^{-i\frac{2\pi}{3}}$ ($e^{i\frac{2\pi}{3}}$) eigenvalue of C_3-rotation. The 2*s*-like basis excitons ϕ_K^{2s} and $\phi_{K'}^{2s}$ from the two valleys have exactly the same symmetry properties as those of the 1*s*-like basis excitons. Although the bright 2*p*-like ($m = 1$ and $m = -1$ for K- and K'-valleys respectively) basis excitons, $\phi_K^{2p_+}$ and $\phi_{K'}^{2p_-}$, have the same representation *E*, the E_+ (E_-) component is in the K'- (K-) valley, which is opposite to the 1*s*- and 2*s*-like basis excitons. When intervalley interactions are taken into considerations, only basis excitonic states (ϕ_K^j and $\phi_{K'}^l$) with both same irreducible representation and the same representation component can be hybridized, as the full BSE Hamiltonian respects the crystal symmetries. Therefore, only 2*p*-like basis exciton in the K- (K'-) valley is allowed to be hybridized with 1*s*- and 2*s*-like excitons in the K'- (K-) valley. Since the energy difference between 1*s*- and 2*p*-like basis excitons is as large as 890 meV compared to a value of 240 meV between the 2*s*- and 2*p*-like states, we expect stronger intervalley coupling between the latter states from different valleys. Indeed, our calculations in the full BZ using a **k**-points sampling 400 × 400 × 1 show that the inclusion of K and K' interactions causes a level repulsion between 2*p*- and 2*s*-like states, with the energy level of 2*p*- (2*s*-) like state decreased (increased) by 30 (28) meV (SM Sec. V) as compared to that in the absence of K and K' interactions, while the energy of the 1*s*-like states remains unchanged [50]. Thus, although intervalley coupling is there, its influence to the energy and character of the excitons is not dominant; we shall therefore continue to denote a true exciton state with the nomenclature of the Rydberg series associated with its corresponding primary basis exciton.

The intervalley 2*p*-2*s* excitonic hybridization can be further seen from Fig. 3, where the square root of the sum of the magnitude square of the envelope functions ($\sqrt{\sum_S |A_k^S|^2}$, here *S* denotes summation over degenerate states) contributing to peaks *A* [Fig. 3(a)], *B* [Fig. 3(b)] and *C* [Fig. 3(c)] from the calculation with inclusion of intervalley interaction are plotted. It is clear peak *A* is still 1*s*-like. While excitons forming peak *B* (*C*) are 2*p*-like (2*s*-like)

without including intervalley interaction (see Fig. 2), the peak now has characteristic of both 2*p*- and 2*s*-like states in the presence of K- and K'-valleys interaction. In particular, for excitons forming peak *B*, the non-zero magnitude of electron-hole pair excitations at exactly the K- or K'-point shown in Fig. 3(b) comes from admixture with the 2*s*-like states; For peak *C*, the nodal structure of 2*s*-state [Fig. 3(c)] disappears due to non-zero electron-hole pairs excitations of 2*p*-like states in the same **k**-points. The intervalley interaction induces hybridization of 2*s*- and 2*p*-like states located in different valleys, making the amplitude of the excitons envelope functions contributing to peak *B* and peak *C* similar as shown in Figs. 3(b) and 3(c), as well as resulting in novel excitonic *s*-*p* hybridization states which were not previously reported.

In conclusion, we have performed first-principles calculations of the electronic and optical properties of monolayer hBN with many-electron interaction effects included, employing the *GW* and *GW*-BSE methods, respectively. We identify and analyze the characters of the exciton peaks in the optical spectrum. The first peak corresponds to 1*s*-like excitons at 5.95 eV with a large binding energy of 2.08 eV. Remarkably, we discovered that the second peak corresponds to bright *p*-like excitons with an excitation energy of 6.84 eV, which is consistent with the CWL optical selection rules [6] for excitons in 2D insulators, but has not previously been characterized correctly in experiment or theory. Also, due to the extended **k**-space envelope function of the excitons, the near perfect circular dichroism seen in monolayer TMDs is no longer present in monolayer hBN, and intervalley coupling of *s*- and *p*-like excitons further leads to symmetry-allowed intervalley *s*-*p* hybridization. We expect that the novel *p*-like excitons and *s*-*p* excitonic hybridization found here would help us to understand excitonic properties of defects in and heterostructures made by hBN layers, as well as open a new avenue for photoelectronics.

References

1. C.-H. Park, and S. G. Louie, Tunable excitons in biased bilayer graphene, *Nano Lett.* **10**, 426 (2010).
2. D. Xiao, W. Yao, Q. Niu, Valley-contrasting physics in graphene: magnetic moment and topological transport, *Phys. Rev. Lett.* **99**, 236809 (2007).
3. D. Xiao, G. B. Liu, W. Feng, X. Xu, and W. Yao, Coupled spin and valley physics in monolayers of MoS_2 and other group-VI dichalcogenides, *Phys. Rev. Lett.* **108**, 196802 (2012).
4. T. Cao, G. Wang, W. Han, H. Ye, C. Zhu, J. Shi, Q. Niu, P. Tan, E. Wang, B. Liu, J. Feng, Valley-selective circular dichroism of monolayer molybdenum disulphide, *Nat. Commun.* **3**, 887 (2012).
5. C. K. Yong *et al.*, Valley-dependent exciton fine structure and Autler–Townes doublets from Berry phases in monolayer $MoSe_2$, *Nat. Mater.* **18**, 1065 (2019).
6. T. Cao, M. Wu, and S. G. Louie, Unifying optical selection rules for excitons in two dimensions: band topology and winding numbers, *Phys. Rev. Lett.* **120**, 087402 (2018).
7. X. O. Zhang, W. Y. Shan, and D. Xiao, Optical selection rule of excitons in gapped chiral fermion systems, *Phys. Rev. Lett.* **120**, 077401 (2018).
8. L. Ju *et al.*, Tunable excitons in bilayer graphene, *Science* **358**, 907 (2017).
9. D. Y. Qiu, F. H. da Jornada, and S. G. Louie, Optical spectrum of MoS2: many-body effects and diversity of exciton states, *Phys. Rev. Lett.* **111**, 216805 (2013).
10. D. Y. Qiu, T. Cao, and S. G. Louie, Nonanalyticity, valley quantum phases, and lightlike exciton dispersion in monolayer transition metal dichalcogenides: theory and first-principles calculations, *Phys. Rev. Lett.* **115**, 176801 (2015).
11. R. Soklaski, Y. Liang, and L. Yang, Temperature effect on optical spectra of monolayer molybdenum disulfide, *Appl. Phys. Lett.* **104**, 193110 (2014).

12. M. Rohlfing, and S. G. Louie, Electron-hole excitations and optical spectra from first principles, *Phys. Rev. B* **62**, 4927 (2000).
13. P. Cudazzo, L. Sponza, C. Giorgetti, L. Reining, F. Sottile, and M. Gatti, Exciton band structure in two-dimensional materials, *Phys. Rev. Lett.* 116, 066803 (2016).
14. T. Galvani, F. Paleari, H. P. C. Miranda, A. Molina-Sánchez, L. Wirtz, S. Latil, H. Amara, and F. Ducastelle, Excitons in boron nitride single layer, *Phys. Rev. B* **94**, 125303 (2016).
15. A. Avsar, H. Ochoa, F. Guinea, B. Özyilmaz, B. J. van Wees, and I. J. Vera-Marun, Colloquium: spintronics in graphene and other two-dimensional materials, *Rev. Mod. Phys.* **92**, 021003 (2020).
16. C. R. Dean *et al.*, Boron nitride substrates for high-quality graphene electronics, *Nat. Nanotech.* **5**, 722 (2010).
17. L. Wang *et al.*, One-dimensional electrical contact to a two-dimensional material, *Science* **342**, 614 (2013).
18. Y. Kubota, K. Watanabe, O. Tsuda, and T. Taniguchi, Deep ultraviolet light–emitting hexagonal boron nitride synthesized at atmospheric pressure, *Science* **317**, 932 (2007).
19. T. T. Tran, K. Bray, M. J. Ford, M. Toth and I. Aharonovich, Quantum emission from hexagonal boron nitride monolayers, *Nat. Nanotech.* **11**, 37 (2016).
20. M. S. Hybertsen, and S. G. Louie, Electron correlation in semiconductors and insulators: Band gaps and quasiparticle energies, *Phys. Rev. B* **34**, 5390 (1986).
21. J. P. Perdew, K. Burke, and M. Ernzerhof, Generalized gradient approximation made simple, *Phys. Rev. Lett.* **77**, 3865 (1996).
22. X. Li, H. Qiu, X. Liu, J. Yin, W. Guo, Wettability of supported monolayer hexagonal boron nitride in air, *Adv. Funct. Mater.* **27**, 1603181 (2017).
23. A. Chernikov, T. C. Berkelbach, H. M. Hill, A. Rigosi, Y. Li, O. B. Aslan, D. R. Reichman, M. S. Hybertsen, and T. F. Heinz, Exciton binding energy and nonhydrogenic Rydberg series in monolayer WS_2, *Phys. Rev. Lett.* **113**, 076802 (2014).
24. J. Deslippe, M. Dipoppa, D. Prendergast, M. V. O. Moutinho, R. B. Capaz, and S. G. Louie, Electron-hole interaction in carbon nanotubes: novel screening and exciton excitation spectra, *Nano Lett.* **9**, 1330 (2009).
25. X. L. Yang, S. H. Guo, F. T. Chan, K. W. Wong, and W. Y. Ching, Analytic solution of a two-dimensional hydrogen atom. I. Nonrelativistic theory, *Phys. Rev. A* **43**, 1186 (1991).
26. See Supplemental Material at *weblink* for (1) computational details; (2) interband optical matrix elements; (3) Massive Dirac-Fermion Hamiltonian and optical selection rules; (4) calculation of helicity parameter; (5) repulsion between 2*p*- and 2*s*-like states due to the intervalley interactions; (6) comparison of **k**-space localization of excitons in monolayer MoS_2 vs. hBN; and (7) effective two-dimensional screening from the Keldysh model, which includes Ref. [27-45].
27. P. Giannozzi *et al*., QUANTUM ESPRESSO: a modular and open-source software project for quantum simulations of materials, *J. Phys. Condens. Matter* **21**, 395502 (2009).
28. D. R. Hamann, Optimized norm-conserving Vanderbilt pseudopotentials, *Phys. Rev. B* **88**, 085117 (2013).
29. T. Sohier, M. Calandra and F. Mauri, Density functional perturbation theory for gated two-dimensional heterostructures: theoretical developments and application to flexural phonons in graphene, *Phys. Rev. B* **96**, 075448 (2017).
30. J. Deslippe, G. Samsonidze, D. A. Strubbe, M. Jain, M. L. Cohen, and S. G. Louie, BerkeleyGW: a massively parallel computer package for the calculation of the quasiparticle and optical properties of materials and nanostructures, *Comput. Phys. Commun.* **183**, 1269 (2012).
31. D. Y. Qiu, F. H. da Jornada, and S. G. Louie, Screening and many-body effects in two-dimensional crystals: Monolayer MoS_2, *Phys. Rev. B* **93**, 235435 (2016).
32. F. H. da Jornada, D. Y. Qiu, and S. G. Louie, Nonuniform sampling schemes of the Brillouin zone for many-electron perturbation-theory calculations in reduced dimensionality, *Phys. Rev. B* **95**, 035109 (2017).

33. H. Şahin, S. Cahangirov, M. Topsakal, E. Bekaroglu, E. Akturk, R. T. Senger, S. Ciraci, Monolayer honeycomb structures of group-IV elements and III-V binary compounds: first-principles calculations, *Phys. Rev. B* **80**, 155453 (2009).
34. F. A. Rasmussen, P. S. Schmidt, K. T. Winther, and K. S. Thygesen, Efficient many-body calculations for two-dimensional materials using exact limits for the screened potential: band gaps of MoS_2, h-BN, and phosphorene, *Phys. Rev. B* **94**, 155406 (2016).
35. I. Guilhon, M. Marques, L. K. Teles, M. Palummo, O. Pulci, S. Botti, F. Bechstedt, Out-of-plane excitons in two-dimensional crystals, *Phys. Rev. B* **99**, 161201 (2019).
36. H. Mishra, and S. Bhattachary, Giant exciton-phonon coupling and zero-point renormalization in hexagonal monolayer boron nitride, *Phys. Rev. B* **99**, 165201 (2019).
37. L. Yang, J. Deslippe, C. H. Park, M. L. Cohen, and S. G. Louie, Excitonic effects on the optical response of graphene and bilayer graphene, *Phys. Rev. Lett.* **103**, 186802 (2009).
38. C. Elias *et al*., Direct band-gap crossover in epitaxial monolayer boron nitride, *Nat. Commun.* **10**, 2639 (2019).
39. J. H. Choi, P. Cui, H. P. Lan; Z. Y. Zhang, Linear scaling of the exciton binding energy versus the band gap of two-dimensional materials, *Phys. Rev. Lett.* **115**, 066403 (2015).
40. P. T. Mahon, R. A. Muniz, and J. E. Sipe1, Quantum interference control of localized carrier distributions in the Brillouin zone, *Phys. Rev. B* **100**, 075203 (2019).
41. D. Xiao, G. B. Liu, W. Feng, X. Xu, W. Yao, Coupled spin and valley physics in monolayers of MoS_2 and other group-VI dichalcogenide, *Phys. Rev. Lett.* **108**, 196802 (2012).
42. A. Kormányos, V. Zólyomi, N. D. Drummond, P. Rakyta, G. Burkard, and V. I. Fal'ko, Monolayer MoS_2: trigonal warping, the Γ valley, and spin-orbit coupling effects, *Phys. Rev. B* **88**, 045416 (2013).
43. Steinhoff, M. Rösner, F. Jahnke, T. O. Wehling, and C. Gies, Influence of excited carriers on the optical and electronic properties of MoS_2, *Nano Lett.* **14**, 3743 (2014).
44. L.V. Keldysh, Coulomb interaction in thin semiconductor and semimetal films, *JETP Lett.* **29**, 658 (1979).
45. F. H. da Jornada, L. Xian, A. Rubio, and S. G. Louie, Universal slow plasmons and giant field enhancement in atomically thin quasi-two-dimensional metals, *Nat. Commun.* **11**, 1013 (2020).
46. Our *GW*-BSE calculations yield a series of triplet excitons with similar orbital characters, and we focus on the singlet excitons here for the optical properties.
47. P. Gong, H. Y. Yu, Y. Wang, and W. Yao, Optical selection rules for excitonic Rydberg series in the massive Dirac cones of hexagonal two-dimensional materials, *Phys. Rev. B* **95**, 125420 (2017).
48. Z. Ye, T. Cao, K. O'Brien, H. Zhu, X. Yin, Y. Wang, S. G. Louie, and X. Zhang, Probing excitonic dark states in single-layer tungsten disulphide, *Nature* **513**, 214 (2014).
49. K. F. Mak, K. He, J. Shan, and T. F. Heinz, Control of valley polarization in monolayer MoS_2 by optical helicity, *Nat. Nanotech.* **7**, 494 (2012).
50. The two degenerate dark *p*-like basis excitons ϕ_K^{2p-} and $\phi_{K'}^{2p+}$ together form the basis states for the 2D reducible representation $A_1 \oplus A_2$, they are linearly combined to form two nondegenerate true exciton dark states (when intervalley interactions are considered): one with energy 6.88 eV of representation A_2, and the other with energy 6.96 eV of representation A_1.

Acknowledgements

This research was supported by the sp2 program at the Lawrence Berkeley National Lab through the Office of Basic Science, U. S. Department of Energy under Contract No. DE-AC02-05CH11231, and by the Science and Technology Development Fund Grant No. FDCT/013/2017/AMJ and the Multi-Year Research Grant No. MYRG-2018-00142-IAPME at University of Macau. This research used resources of the Extreme Science and Engineering Discovery Environment (XSEDE) which is supported by National Science Foundation Grant No. ACI-1548562 &

Grant No. DMR-1926004, and Center for Computational Science and Engineering of Southern University of Science and Technology with Grant No. 2019B030301001.

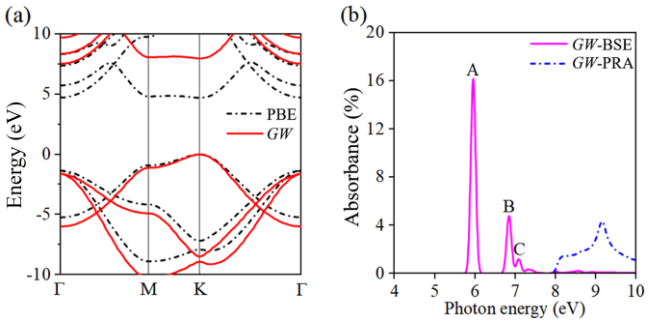

FIG. 1. (a) DFT-PBE (dash black) and full-frequency eigenvalue-self-consistent *GW* (solid red) band structures. The top of the valence band is set at 0 eV. (b) Calculated absorption spectrum with (*GW*-BSE, solid pink) and without (*GW*-RPA, dash blue) electron-hole interactions for linear-polarized light. The first three peaks are labeled as *A*, *B* and *C*, respectively. A gaussian broadening factor of 100 meV is included.

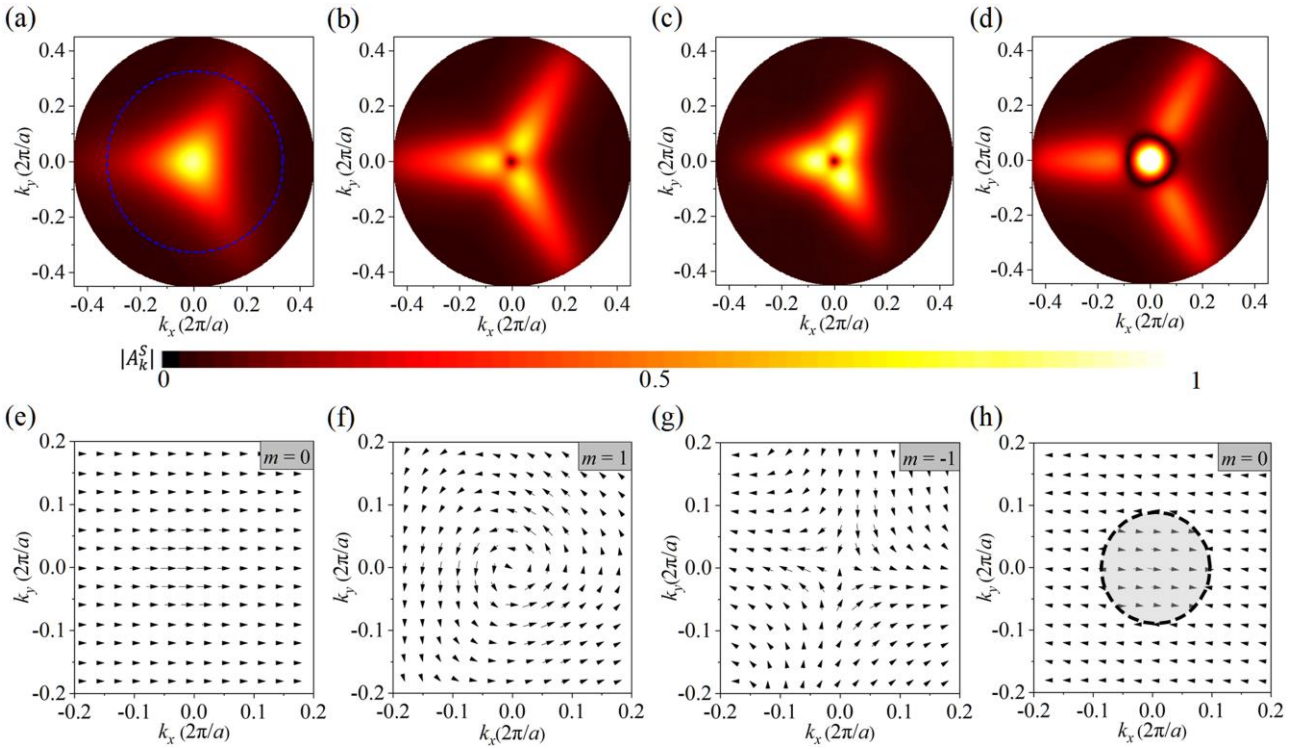

FIG. 2. Calculated amplitude and phase in **k**-space of the envelope function $A_{\boldsymbol{k}}^{S}$ for the first four lowest energy singlet excitons, from a calculation restricting coupling only of interband transitions within the K-valley region. The amplitude of $A_{\boldsymbol{k}}^{S}$ of the state corresponding to (a) peak *A*, (b) peak *B*, (c) a dark exciton near peak *B*, and (d) peak *C*, as labeled in Fig.1. The amplitude indicates the magnitude of the free electron-hole pair excitation at each **k**-point. The plotted value of each point has been normalized to its overall largest value in the BZ. The color scale-bar is shown under panels (a)-(d). The phase of $A_{\boldsymbol{k}}^{S}$ is presented for states in (e) peak *A*, (f) peak *B*, (g) a dark exciton near peak *B*, and (h) peak *C*. The angle of the arrows with respect to the k_x-direction gives the phase of $A_{\boldsymbol{k}}^{S}$. Length of arrows' tail represents the relative amplitude of $A_{\boldsymbol{k}}^{S}$. The winding number about the *K*-point, m, denotes the angular quantum number of $A_{\boldsymbol{k}}^{S}$. All plots use Cartesian coordinates where the origin is set at K-point. The blue dashed circle in (a) has radius $\frac{1}{3}\cdot\frac{2\pi}{a}$. The black dashed circle in (h) highlights the nodal structure as seen in (d). Note that the **k**-space regions in (a-d) are different from those in (e-h).

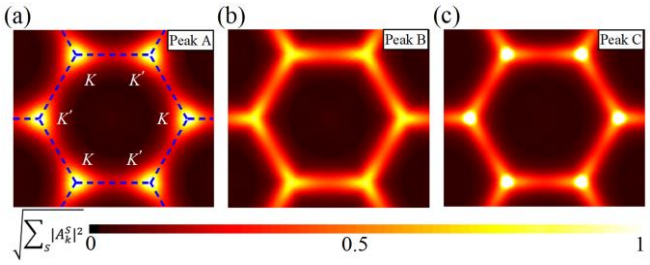

FIG. 3. Calculated amplitude of the envelope function $A_{\boldsymbol{k}}^{S}$ of bright excitons contributing to the first three peaks in the optical absorption spectrum of monolayer hBN, in the presence of K- and K'-valley interaction. The square root of the sum of amplitude square of excitons corresponding to (a) peak *A*, (b) peak *B*, and (c) peak *C* in the full BZ region, normalized to its overall largest value with the color scale-bar shown below the panels. The summation index *S* represents degenerate bright excitonic states.